Applied Surface Science 613 (2023) 156024

Contents lists available at ScienceDirect

Applied Surface Science

journal homepage: www.elsevier.com/locate/apsusc

Full length article

Strengthening the Ti/TiN interface against shear failure with Al dopants: A molecular dynamics study

Nisha Dhariwal [a], Abu Shama Mohammad Miraz [a], W.J. Meng [b], Collin D. Wick [a,*]

[a] College of Engineering & Science, Louisiana Tech University, Ruston, LA 71272, USA
[b] Department of Mechanical & Industrial Engineering, Louisiana State University, Baton Rouge, LA 70803, USA

ARTICLE INFO

Keywords:
MEAM
Molecular dynamics
Metal/ceramic interfaces
Doping
Shear strength
Misfit dislocations

ABSTRACT

The impact of Al doping on the stability and shear strength of the Ti/TiN interface was investigated using a newly developed modified embedded atom model interatomic potential. The model was parameterized to the interfacial properties of pure Al, TiAl and AlN binaries as well as TiAlN ternary system. The results of the new model are in reasonably good agreement with those obtained using Density Functional Theory and experimental data from the literature. A Ti/TiN system with a misfit dislocation network present on the Ti layer adjacent to the TiN interface was chosen for doping because of its low interfacial energy. To find the most likely configuration of Al atoms in Ti/TiN, a Monte Carlo scheme was developed. A range of Al compositions were studied, in which higher Al composition caused a more negative enthalpy of mixing up to 25 mol%. Even at small Al compositions, a drastic increase in shear strength was observed, continuously increasing with increasing Al composition. The highest Al composition had an abundance of screw dislocations, which were found to be responsible for its high shear strength.

1. Introduction

The study of metal/ceramic interfaces is an active area of research due to its applications in a wide variety of fields such as in microelectronic packaging, wear-resistant materials, electronic devices, fiber-matrix composites, sensors, medical implants, and thermal barrier coatings [1–9]. Ceramics exhibit good resistance to wear and oxidation, while metals are ductile and possess good electrical and thermal properties [10]. Mechanical response of metal/ceramic systems is often controlled by the interface; hence, a complete knowledge of the structure and mechanical behavior of the metal/ceramic interfaces can enable material engineers to make a better choice of materials in order to design stable systems with a desired strength [11]. There has been a growing interest in the study of adhesion between metals and ceramics for many years [12]. With increasingly capable experimental probes, such as high-resolution transmission electron microscopy and electron energy loss spectroscopy, the atomic and chemical structure of the interfaces can be investigated to near atomic resolution [9]. However, obtaining a detailed understanding of interfacial interactions remains a challenge [13]. The behavior of metal/ceramic interfaces at the atomic level can be understood more precisely through atomic level simulations such as first principles density functional theory (DFT) [14–16].

An important consideration is the presence of impurities or dopant atoms and its impact on the properties of metal/ceramic interfaces. Dopants have been known to affect the bonding and cohesion at imperfections such as grain boundaries of metal/ceramic interfaces [17–19]. They have also been found to impact the adhesion at metal/ceramic interfaces [13],[20–24]. A number of first principles calculations have been done to study the interfacial properties of metal/ceramic systems, including the introduction of transition metal dopants to the interface [25],[26]. In a recent first principles study, it was observed that the addition of Al to the Ti/TiN interfacial region significantly increased the generalized stacking fault energy (GSFE) barrier by drawing some of the electron charge from the ceramic N atoms into the Ti phase [10]. However, DFT is limited to the study of small sized systems due to the associated high computational cost [27]. In order to study more complex interfacial effects, such as how misfit dislocation networks (MDNs) affect interfacial mechanical properties, larger system sizes are required. Such larger scale simulation studies will allow generation of insights that are more closely related to experimental observations. In particular, large-scale molecular dynamics (MD) simulations can be utilized [28] to bring system sizes to the order of millions of

* Corresponding author.
E-mail address: cwick@latech.edu (C.D. Wick).

https://doi.org/10.1016/j.apsusc.2022.156024
Received 7 October 2022; Received in revised form 15 November 2022; Accepted 6 December 2022
Available online 10 December 2022

atoms.

One of the main challenges in carrying out large-scale MD simulations is the need for appropriate interatomic potentials that can accurately describe the system of interest. Modified embedded atom method (MEAM) potentials have been extensively utilized for metallic systems [29–36], along with different ceramics, such as TiN and CrN [37–39]. Employing MEAM potentials, several metal/ceramic interfaces have been recently studied to provide a detailed understanding on the interfacial stability, the influence of MDNs, the shear strength [40–42], as well as mechanisms of epitaxial growth of metal on a ceramic template [43]. Based on the above considerations and extending previous work [10], this paper describes the development of a new MEAM potential for Ti-Al-N ternary systems. The new model was used to investigate how the addition of Al dopants impacts the structure and shear strength of the Ti/TiN interface.

2. Methodology

2.1. Interatomic potential

A detailed description of MEAM formalism has been covered in the literature [44. Briefly, the total energy of a system is estimated as the sum of an embedding function, F_i, and a pair interaction, $\varphi_{ij}(R_{ij})$, between atoms i and j at a distance R_{ij},

$$E_{\text{total}} = \sum_i \left[F_i(\overline{\rho}_i) + \frac{1}{2}\sum_{j\neq i} S_{ij}\varphi_{ij}(R_{ij}) \right] \quad (1)$$

$$F(\overline{\rho}) = AE_c\left(\overline{\rho}/\overline{\rho}^0\right) ln\left(\overline{\rho}/\overline{\rho}^0\right) \quad (2)$$

where A is an adjustable parameter, E_c is the sublimation energy, and $\overline{\rho}^0$ is the background electron density for a reference structure. S_{ij} is the screening function between atoms, which will be described later. The background electron density at site i is $\overline{\rho}$, which is constituted by partial electron density terms for different angular contributions [34]. The partial electron densities are combined as follows:

$$\overline{\rho}_i = \rho_i^{(0)} G(\Gamma) \quad (3)$$

where

$$G(\Gamma) = 2/(1+e^{-\Gamma}) \quad (4)$$

and

$$\Gamma = \sum_{h=1}^{3} t_i^{(h)} \left[\rho_i^{(h)} \Big/ \rho_i^{(0)} \right]^2 \quad (5)$$

$t_i^{(h)}$ are the adjustable parameters. The atomic electron densities are given as

$$\rho_j^{(h)}(R) = \rho_0 e^{-\beta^{(h)}\left(\frac{R}{r_e}-1\right)} \quad (6)$$

which involves the adjustable parameters $\beta^{(0)}$, $\beta^{(1)}$, $\beta^{(2)}$, $\beta^{(3)}$ and r_e, the nearest neighbor distance in the equilibrium reference structure. The energy per atom for a given reference structure is calculated from the universal equation of state by Rose et al. [45],

$$F\left[\overline{\rho^0}(R)\right] + \frac{1}{2}\sum \phi(R) = E^u(R) = -E_c\left(1 + a^* + a_3 a^{*3}\right)e^{-a^*} \quad (7)$$

where

$$a^* = \alpha\left(\frac{R}{r_e} - 1\right) \quad (8)$$

$$a_3 = d_{repuls}, a^* < 0 \text{ and } a_3 = d_{attrac}, a^* \geq 0 \quad (9)$$

α is an adjustable parameter involving contributions from the bulk modulus, cohesive energy, and equilibrium atomic volume. S_{ij}, as given in Eq. (1), is a many-body screening function that denotes the effect of the position of an atom k on the interaction between atoms i and j, which is limited by C_{min} and C_{max} as described in detail in a previous work [46]. A value of $S_{ij} = 1$ implies that the interaction between atoms i and j is unscreened while a value of $S_{ij} = 0$ means that the interaction is completely screened. The cutoff distance of 5 Å was used in this work to be compatible with the model used for Ti/TiN [40].

For pure elements, 13 MEAM parameters are required to be determined: $\beta^{(0)}$, $\beta^{(1)}$, $\beta^{(2)}$, $\beta^{(3)}$, $t^{(1)}$, $t^{(2)}$, $t^{(3)}$, A, α, E_c, r_e, C_{min}, and C_{max}. Normally, the equilibrium structure is taken as the reference structure and E_c and r_e values are set to experimental values. The reference structures for Ti and Al are hcp and fcc, respectively, and the MEAM parameters for N were taken from the literature without any modification [39]. For each binary system there are 11 additional parameters that are required to be fit, including E_c in Eq. (2), α and r_e values in Eq. (8), four C_{min}, and four C_{max} values. For ternary interactions, an additional six parameters, three C_{min} and three C_{max}, are fit. For the pure Ti and the binary TiN system, the previously developed model designed to study the Ti/TiN interface was used [40]. We parameterized a model for pure Al and compared it with one developed by Lee et al. [47], along with a model for the binary combinations Al—N and Ti—Al (Ti—N was taken from a previous work [40]), and for the ternary combination of Ti-Al-N. The optimization of a set of MEAM parameters was done by utilizing a Python code developed by our group based on minimizing the mean square displacement between the calculated and the experimental/DFT derived properties with the aid of a genetic algorithm [48].

2.2. DFT calculations

The Vienna ab initio simulation package [49] was utilized for the DFT calculations using the Perdew, Burke, and Ernzerhof generalized gradient approximation for the exchange-correlation functional [50], [51]. The potential due to the core electrons was accounted for by the projector augmented wave method [52], which combines the features of the pseudopotential approach and the linear augmented plane wave method. Kohn-Sham orbitals for valence electrons were expanded in terms of a plane wave basis set with a cutoff energy of 400 eV. The Monkhorst-Pack scheme was used for sampling the k-point of the plane wave basis in the first Brillouin zone [53] and in the calculations, the specific k-point mesh size used was based on the system size. The monovacancy formation energy, surface energies, and the GSFEs for pure Al were calculated using first-principles DFT. In order to calculate the monovacancy formation energy, the Brillouin zone was sampled using 4 × 4 × 4 mesh of k-points for the 32-atom cells. The surface energies were calculated for the surfaces Al(001), Al(110), and Al(111) with the system sizes of 36, 32, and 24 atoms, respectively, and the Brillouin zone was sampled using a 4 × 4 × 1 k-point mesh. For each of these surfaces, a periodic system with a 15 Å of vacuum was created, resulting in the formation of two surfaces.

The GSFE surface was calculated for the Al(001) and Al(111) planes. For both, a system of 48 atoms was used with 12 layers of 4 atoms each with 15 Å of vacuum present. In the Al(001) GSFE calculation, half of the atoms were displaced in the X[110] and Y[$\bar{1}$10] directions, while for Al (111), the displacements were in the X[001] and Y[00$\bar{1}$] directions, keeping the other half of atoms fixed as had been done previously [54]. A total of ten positions along X and ten along the Y directions were sampled, mapping a total of 100 points. For each point, an energy minimization followed their displacement, allowing the atoms to only relax in the Z direction (keeping X and Y positions all fixed). The minimum energy path was then plotted along the X direction after mapping the full GSFEs out, which will be denoted 1D-GSFE [10]. The maximum height of the minimum energy plot gives the energy barrier of the shear displacement of the GSFE surfaces.

The binary systems had their elastic constants, surface energies, and the enthalpies of mixing calculated using DFT. The elastic constants were calculated using a system size of 64 atoms for TiAl, 24 atoms for $TiAl_3$ and 24 atoms for Ti_3Al with a 12 × 12 × 12 k-point mesh. To calculate the enthalpy of mixing, a Ti_3Al system of 24 atoms, a $TiAl_3$ system of 32 atoms and a TiAl system of 32 atoms were used, each with a 4 × 4 × 4 k-point mesh. For the surface energy calculations, 48, 44 and 72 atoms were used for TiAl(001), TiAl(110) and TiAl(111). In each of these systems, 15 Å of vacuum were present normal to the surface in consideration, and a k-point grid of 4 × 4 × 1 was used for all the cases. The impact of spin-polarized calculations was investigated for all the systems, and it was found that they did not have a significant impact on the structure and energetics of these systems.

The GSFE calculations of the interfacial systems were carried out in a previous work [10]. The metal phase included 16 layers of 4 atoms (64 total metal atoms) with its (0001) surface in contact with the (111) surface of 6 layers of TiN (48 total atoms) with the N atoms oriented towards the Ti phase. As with the metal GSFE calculations, 15 Å of vacuum was present. The value, which will be referred to as M, describes the metal layer away from the TiN surface. Three different system configurations were used for the GSFE calculations: a system with one Al atom in the M = 1 layer, a system with two atoms in the M = 2 layer, and a system with 16 Al atoms (1/4 of the metal atoms), which were distributed based on a Monte Carlo minimization scheme [10]. The determination of the GSFE was carried out by displacing the atoms along the X and Y planes in 10 increments each (see ref. [10] for the specific directions and further details). The plane in which the displacement occurred was in between the M = 1 and M = 2 surface layers in the metal phase, which had the lowest barrier for the Ti/TiN interface.

2.3. Calculation of properties from the MEAM model

The LAMMPS simulation software [55] was used to calculate all of the MEAM properties. For Al, the lattice constants, the energy ratio of different crystal structures with respect to the most stable structure, i.e. (E_{bcc}/E_{fcc}) and (E_{hcp}/E_{fcc}), surface energies (E_s) of various surfaces Al (001), Al(110), Al(111), solid density (ρ_s), elastic constants, and monovacancy formation energy (E_{vac}) were calculated. For all calculations except the solid density, energy minimizations were carried out with the conjugate gradient method. The fcc system had 108 atoms, the hcp system had 48 atoms, and the bcc system had 54 atoms. To calculate the monovacancy formation energy for Al, one atom was removed from the fcc system of 108 atoms. The elastic constant calculations were carried out for the fcc system with 108 atoms, and systems with 72, 48, and 48 atoms were used for the calculation of surface energies of Al(001), Al (110), and Al(111) surfaces, respectively. To calculate the solid density for Al metal, 20 ps of NPT simulations of a system with 500 atoms were carried out at 298 K and 1 atm using the Nosè-Hoover thermostat and barostat [56],[57] with a timestep of 1 fs.

For binary systems, the enthalpy of mixing was calculated for TiAl, $TiAl_3$ and Ti_3Al. The enthalpy of mixing was calculated using a system of 128 atoms for TiAl, 64 atoms for Ti_3Al and a system of 64 atoms for $TiAl_3$. The surface energies were calculated using a system size of 72 atoms for both TiAl(001) and TiAl(100), 64 atoms for TiAl (110) and 54 atoms for TiAl (111) surfaces. The elastic constants were calculated using 36 atoms for TiAl, and 64 atoms for both Ti_3Al and $TiAl_3$. For ternary systems, the enthalpy of mixing and lattice parameters were calculated using 216 atoms for Ti_2AlN and 40 atoms for Ti_3AlN. The surface energy for the Ti_2AlN(0001) hexagonal system was calculated using 32 atoms, and 40 atoms for Ti_2AlN(001), 80 atoms for Ti_2AlN(110) and 112 atoms for Ti_2AlN(111) system. The elastic constants for the Ti_2AlN and Ti_3AlN systems were calculated using 96 atoms and 40 atoms, respectively. The GSFEs were calculated using the same system sizes as used in DFT calculations described in Section 2.2.

2.4. Large scale simulations

In this work, the orientation with the lowest energy found in previous work for Ti/TiN was used [40]: X || $[11\bar{2}0]_{Ti}$ || $[1\bar{1}0]_{TiN}$; Y|| $[\bar{1}100]_{Ti}$ || $[11\bar{2}]_{TiN}$, and Z || $[0001]_{Ti}$ || $[111]_{TiN}$. To minimize the lattice mismatch between the metal and the ceramic at the interface for the Ti/TiN system, previous work found that the length of the X and Y dimensions can be set to 16.1 nm and 27.9 nm, respectively [40]. The thickness of the ceramic phase in the Z dimension was approximately 29 Å, while the metal phase was 50 Å. The Z dimension had non-periodic boundary conditions, while the X and Y dimensions were periodic. Also, the previous work found that the interfacial energy was lowest when an MDN was present on the second Ti layer with respect to the TiN surface [40] (with N atoms in contact with the Ti metal), so that was the configuration used in this study (see reference for a detailed description of the formation of dislocations). A total of 133,100 atoms in the metal phase and 69,984 Ti and N atoms combined in the ceramic phase were used in the simulation.

A number of the Ti atoms in the metal phase were replaced with Al atoms, giving mol % ranging from 1 to 25%. It should be noted that 25% Al means that 25% of the 133,100 Ti atoms in the metal phase (not the ceramic) were replaced (33275). To find the most likely configuration for these atoms, a Monte Carlo (MC) scheme was developed as follows:

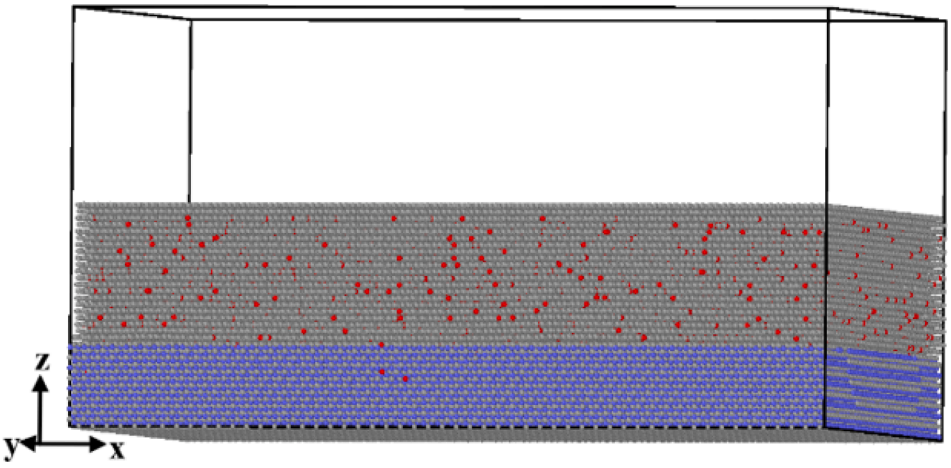

Fig. 1. Snapshot of the Al doped Ti/TiN system snapshot with 4 mol% of Al with gray representing Ti, blue N, and red Al. (For interpretation of the references to colour in this figure legend, the reader is referred to the web version of this article.)

Table 1
MEAM potential parameters for Ti-Al-N.

	E_c (eV)	r_e (Å)	A	α	$\beta^{(0)}$	$\beta^{(1)}$	$\beta^{(2)}$	$\beta^{(3)}$	$t^{(1)}$	$t^{(2)}$	$t^{(3)}$	C_{min}	C_{max}
Al	3.36	1.43	0.89	4.47	2.15	4.62	7.01	0.0	−1.82	−1.02	9.07	0.39	2.24
Ti[a]	4.87	2.92	1.19	4.41	1.58	0.08	2.89	0.0016	5.55	6.79	−2.05	0.89	2.85
N[b]	4.88	1.10	1.80	5.96	2.75	4.00	4.00	4.00	0.05	1.00	0.00	2.00	2.80

[a] Ref. [60].
[b] Ref. [39].

Table 2
Comparison of the DFT calculated/experimental properties of Al with values obtained using the Lee model [47] and the newly developed model in this work.

Property	DFT/expt value	New model	Lee model [47]
Lattice parameters (Å)	4.049	4.050	4.044
	4.049	4.050	4.044
	4.049	4.050	4.044
E_{vac} (eV)	0.78[a], 0.68[b]	1.046	0.6788
E_s (111) (J/m^2)	1.14[a]	0.874	0.6263
E_s (100) (J/m^2)	1.366[a]	1.069	0.8545
E_s (110) (J/m^2)	1.433[a]	1.254	0.9152
Elastic constants (GPa)			
C_{11}	114[a]	95.1	114.33
C_{12}	62[a]	60.2	61.915
C_{44}	32[a]	32.6	31.566
ρ_s (g/cm^3)	2.70[c]	2.697	2.7182
E_{bcc}/E_{fcc}	0.971[a]	0.9882	0.9647
E_{hcp}/E_{fcc}	0.994[a]	0.9975	0.9912

[a] DFT calculated in this work.
[b] Ref [61].
[c] Ref [62]].

1) The Al atoms were placed randomly in the Ti metal phase excluding the top two layers, followed by an energy minimization.
2) Each MC move attempted to exchange 5 atoms (*nexchange*) using Rosenbluth sampling to reduce the number of energy calculations required. The Ti and Al atoms that were chosen for exchange included all atoms not present in the top two or bottom two layers of the entire system (the Ti atoms in the ceramic phase, excluding its bottom two layers, were allowed the exchange).
3) For each atom exchange attempt, a total of 10 trials (*ntrial*) were attempted. The acceptance probability for each trial was carried out with the following probability.

$$P_{acc}^{trial} = \frac{P_i}{\sum_j P_j} \tag{10}$$

where the sum of j is over *ntrial*. How each p_i was determined will be described below.

4) After the *nexchange* exchange attempts were carried out, a single energy minimization was carried out, and if the energy was lower than the energy before the exchanges were attempted, then the entire MC move was accepted.

If the goal were to sample the system at a specific state (i.e., with a set temperature and pressure), the biasing used for the trials would need to be accounted for in the final acceptance. Since the goal is to find the minimum energy of the system (the most stable configuration), this is not necessary. The p_i values used to bias the trialed atomic exchanges was generated by the identity of the 12 nearest neighbors around each atom type. For instance, in bulk Ti doped with Al, there will be an average number of Al atoms and Ti atoms surrounding each Al atom. The biasing probabilities were constantly updated throughout the simulation based on the attempted moves that were accepted. This was used to better guide which of the *ntrial* attempts were more likely to lower the system's energy. In essence, when an MC move was accepted, the environment surrounding the exchanged Ti and Al atoms in the accepted configurations are used to update p_i. Fig. 1 gives a representative configuration with 4 mol% of Al in Ti. As can be observed, the Al atoms are distributed throughout the system, including the ceramic phase as well, albeit in a much lower composition than in the metal phase.

3. Results and discussion

3.1. Pure Al metal

The parameters for the Al MEAM model developed for this work are shown in Table 1. A comparison of the DFT calculated/experimental properties with values obtained using an existing model (Lee model) [47] and the model developed for this work are given in Table 2. The values for E_c and r_e for Al were taken from the experimental values in the literature [58],[59]. From Table 2, it can be observed that reasonable agreement with experimental/DFT values was achieved with both MEAM models. The fcc structure was found to be the most stable, and the correct order among the low index surface energies was achieved for

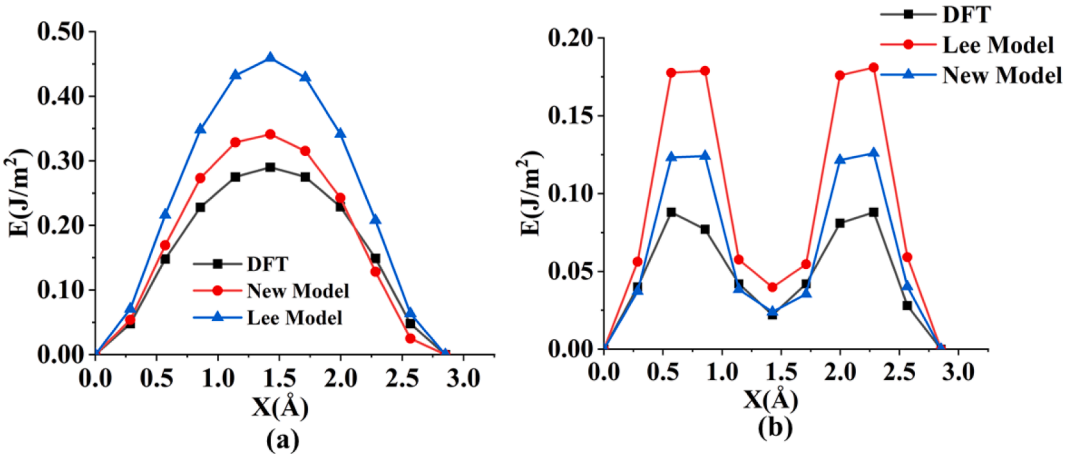

Fig. 2. Comparison of the 1D-GSFEs for pure Al from DFT, the new MEAM model, and the Lee model along the (a) (001) and (b) (111) planes.

Table 3
MEAM potential parameters for the binary systems (*x*-*y*). In any pair, the first element is denoted by *x*, and the second element is denoted by *y*.

Parameters	(*x*-*y*) Pair		
	Ti-Al	N-Al	Ti-N [40]
Reference state	b2	b1	b1
E_c (*x*, *y*) (eV)	4.844	6.53	6.6139
r_e (*x*, *y*) (Å)	3.023	1.6258	2.1195
α (*x*, *y*)	4.022	6.8183	4.7225
C_{min} (*x*, *x*, *y*)	2	0.7183	0.4263
C_{min} (*y*, *y*, *x*)	1.409	0.3414	1.0733
C_{min} (*x*, *y*, *x*)	0.055	0.8582	1.5
C_{min} (*x*, *y*, *y*)	0.936	1.1618	1.5
C_{max} (*x*, *x*, *y*)	4	3.3405	2.0328
C_{max} (*y*, *y*, *x*)	2.133	2.5308	1.7998
C_{max} (*x*, *y*, *x*)	2.644	3.2418	2.4073
C_{max} (*x*, *y*, *y*)	2.993	3.9408	2.3557

Table 4
MEAM potential parameters for the Ti-Al-N ternary interactions.

Parameters	Value
C_{min} (Ti, Al, N)	0.0848
C_{min} (Ti, N, Al)	1.2438
C_{min} (Al, N, Ti)	1.5301
C_{max} (Ti, Al, N)	2.517
C_{max} (Ti, N, Al)	2.4209
C_{max} (Al, N, Ti)	3.1322

Table 5
Comparison between the results of the new model and the experimental/DFT results for TiAl binary systems.

Property	System		Expt/ DFT	New model	Lee model [47]
ΔH_{mix} (eV/ atom)	γ-TiAl (P4/ mmm $L1_0$)		−0.258[a]	−0.237	−0.141
	Ti_3Al (P6_3/ mmc)		−0.279[a]	−0.313	−0.029
	$TiAl_3$ (I4/ mmm)		−0.398[a]	−0.435	−0.163
Elastic constants (GPa)	γ-TiAl (P4/ mmm $L1_0$)	C_{11}	187[b]	192	190
		C_{12}	74.8	83	67
		C_{13}	74.8	111	133
		C_{33}	182	224	234
		C_{44}	109	172	86
		C_{66}	81.2	52	52
	Ti_3Al (P6_3/ mmc)	C_{11}	183.2[c]	241	200
		C_{12}	89	95	107
		C_{13}	62.6	56	91
		C_{33}	225.1	286	238
		C_{44}	64.1	67	45
		C_{66}	47.1	73	46
	$TiAl_3$ (I4/ mmm)	C_{11}	217.7[d]	202	152
		C_{12}	57.7	105	138
		C_{13}	45.5	90	116
		C_{33}	217.5	188	154
		C_{44}	92	100	71
		C_{66}	116.5	143	87
E_S (J/m^2)	γ-TiAl (P4/ mmm $L1_0$)	−1	2.16[e]	1.92	2.43
		−110	1.64[e]	0.64	1.8
		−111	1.79[e]	1	1.98
		−100	2.03[e]	1.75	2.09

[a] Ref [63].
[b] Ref [64].
[c] Ref [65].
[d] Ref [66].
[e] DFT calculated in this work.

Table 6
Comparison between the results of the new model and the DFT results for TiAlN ternary systems.

Property	System		DFT	New model
Lattice parameters	Ti_2AlN (P6_3/mmc)		8.98	8.9
			7.77	7.71
			40.83	41.34
	Ti_3AlN (pm-3 m)		8.22	8.2
			8.22	8.2
			8.22	8.2
ΔH_{mix} (eV)	Ti_2AlN (P6_3/mmc)		−1.32	−1.21
	Ti_3AlN (pm-3 m)		−1	−1.14
Elastic constants (GPa)	Ti_2AlN (P6_3/mmc)	C_{11}	305	234
		C_{12}	67	96
		C_{13}	93	105
		C_{33}	281	322
		C_{44}	123	109
		C_{66}	119	69
	Ti_3AlN (pm-3 m)	C_{11}	202	335
		C_{12}	144	55
		C_{13}	–	–
		C_{33}	–	–
		C_{44}	60	177
		C_{66}	–	–
E_S (J/m^2)	Ti_3AlN (pm-3 m)	−1	1.69	1.76
		−110	2.32	2.12
		−111	1.83	1.95
	Ti_2AlN (P6_3/mmc)	(0001)	2.208	1.87

both models. Figs. S1 and S2 in the supporting information show detailed GSFEs of Al(001) and Al(110) surfaces calculated by DFT, the new MEAM model, and the Lee model [47]. The 1D-GSFEs plots as a function of position along the x-axis is shown in Fig. 2. The new model overpredicts the DFT barrier height in the 1D-GSFE for both surfaces, but only by a modest amount. It should be noted that better agreement with the GSFEs could not be achieved without doing significantly worse on reproducing other properties such as lattice constants, cohesive energy, and elastic constants.

3.2. Mixed systems

The binary parameters for TiAl, Ti_3Al, and $TiAl_3$ were fit to several properties, including enthalpies of mixing, elastic constants, and surface energies. Tables 3 and 4 show the values of the binary and ternary parameters obtained in the present work, respectively, while the Ti—N binary parameters have been taken from our previous work [40]. The DFT and the MEAM calculated values of the various properties of binary and ternary Ti-Al-N systems using the present model are presented in Tables 5 and 6. As can be seen in Tables 5 and 6, there is reasonable agreement between the results of the presented model and DFT/experimental values for TiAl and Ti-Al-N systems. Some of the surface energies for TiAl, in particular, are an exception to this, as improving them came at the expense of worse agreement for the GSFEs of Al doped Ti and Ti/TiN. Agreement for the GSFEs was a major focus of the parameterization, for reasons that are described later.

Previous work showed that with two Al atoms in adjacent layers of bulk Ti, the enthalpy of mixing significantly lowered, and the GSFEs had a significant increase in barrier height [10]. Because of these reasons, this system was a focus of the parameterization strategy for the new model. Fig. 3 gives a snapshot of the system in which the GSFE was extracted, along with the associated 1D-GSFE (See Fig. S3 in the supplementary information for the full GSFE). The plane in which the GSFE was calculated is between the two Al atoms in the X and Z directions in Fig. 3(a). The 1D-GSFE has a more complex structure than the ones extracted from the pure phases, and the new model does a reasonable job of reproducing it.

Fig. 4 shows comparisons of the 1D-GSFEs between the M = 1 and M = 2 metal layers in the Al doped Ti/TiN interfacial systems for DFT and

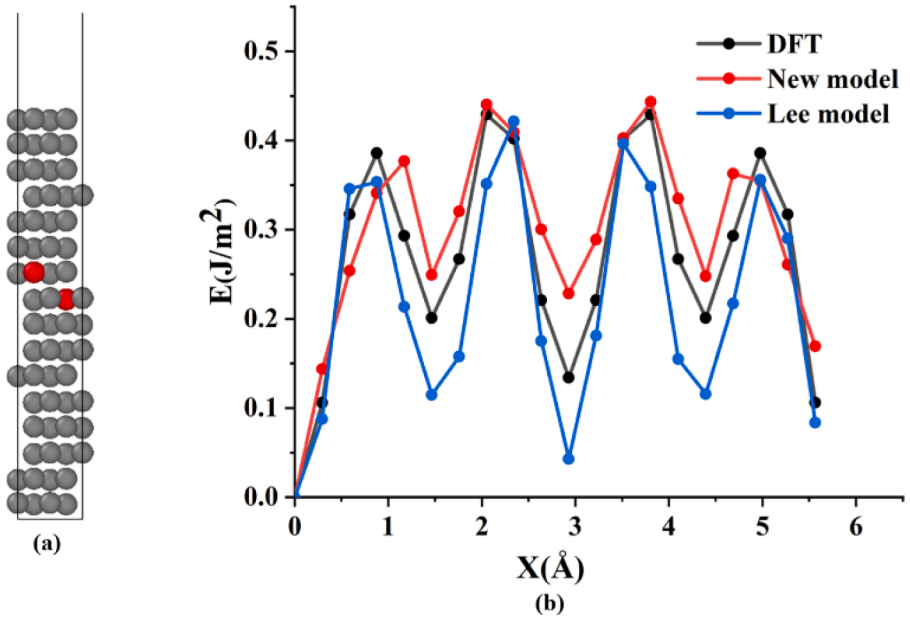

Fig. 3. (a) Snapshot of the Al (red atoms) and Ti (gray atoms) used to calculate the GSFE. (b) Comparison of DFT, the new model and the Lee model [47] 1D-GSFE for this system. (For interpretation of the references to colour in this figure legend, the reader is referred to the web version of this article.)

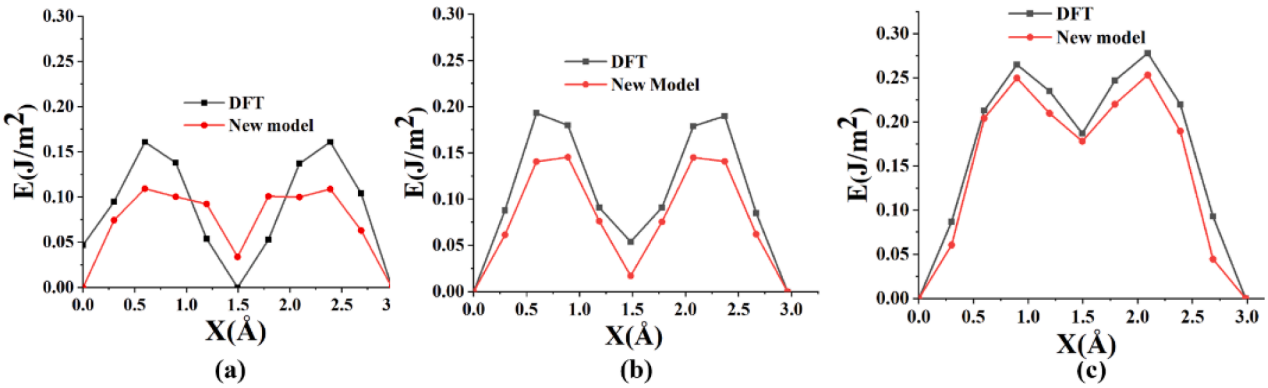

Fig. 4. Comparison of the 1D-GSFE for Ti/TiN with (a) 1 Al atom in the M = 1 layer (b) 2 Al atoms in the M = 2 layer (c) 16 Al atoms, extracted from MC calculations.

the new model. The three systems are those with a single Al atom (Fig. 4 (a)), two Al atoms (Fig. 4(b)), and 16 Al atoms, or 25% of the metal atoms (Fig. 4(c)). The full GSFEs for these systems, along with snapshots of their structures, are given in Figs. S4-S6 in the supporting information. The agreement is not particularly good for the system with one Al atom but is significantly better for the two systems containing two or more Al atoms. This was due to a greater emphasis being placed on parameterizing to systems with more Al atoms than the one with only one Al atom. There is reasonable agreement between the new model and DFT for the system with two Al atoms, while the agreement for the system with 16 Al atoms is particularly good. Overall, the new model somewhat underestimates the 1D-GSFE barrier, but agreement improves with higher Al composition, where the barrier heights increase to a value of approximately 0.28 J/m^2.

3.3. Large scale simulations

3.3.1. Structure and stability

The purpose of the MC simulations was to find low energy configurations. As stated before, the most stable structure for Ti/TiN is the one with an MDN in the M = 2 layer (or the second metal layer from the TiN phase, with N atoms in contact with the Ti metal). Because of this, all large-scale simulations included an MDN in the same position. Fig. 5(a) gives a plot of the energy with respect to MC step for the different systems studied, and it can be observed that a rapid decrease in energy happens at the initial steps, tending to a steady value at higher numbers of steps. Also, the reduction in total energy occurs more rapidly for the cases with higher Al compositions due to its lower overall cohesive energy. To compare the stability of the different systems, the enthalpy of mixing is a better measure, which is calculated as follows when there are n Al atoms exchanged with Ti atoms,

$$\Delta H_{\text{mix}} = E_{\text{doped}} - E_{\text{undoped}} + nE_{\text{Ti}} - nE_{\text{Al}} \tag{11}$$

where E_{undoped} is the Ti/TiN system, and the E_{Al} and E_{Ti} are the energies for bulk Al and Ti systems, respectively. Fig. 5(b) gives the enthalpy of mixing as a function of Al composition after the 5000 MC steps were completed for each system. Unlike the total system energy, the enthalpy of mixing decreases with increasing Al composition until 25 mol% is reached, and after that it increases.

To demonstrate the distribution of Al atoms at the doped Ti/TiN interface, the relative Al composition as a function of position with respect to the interface is plotted in Fig. 5(c). Layer one is the Ti layer immediately next to the TiN phase (with the N atoms in contact with the

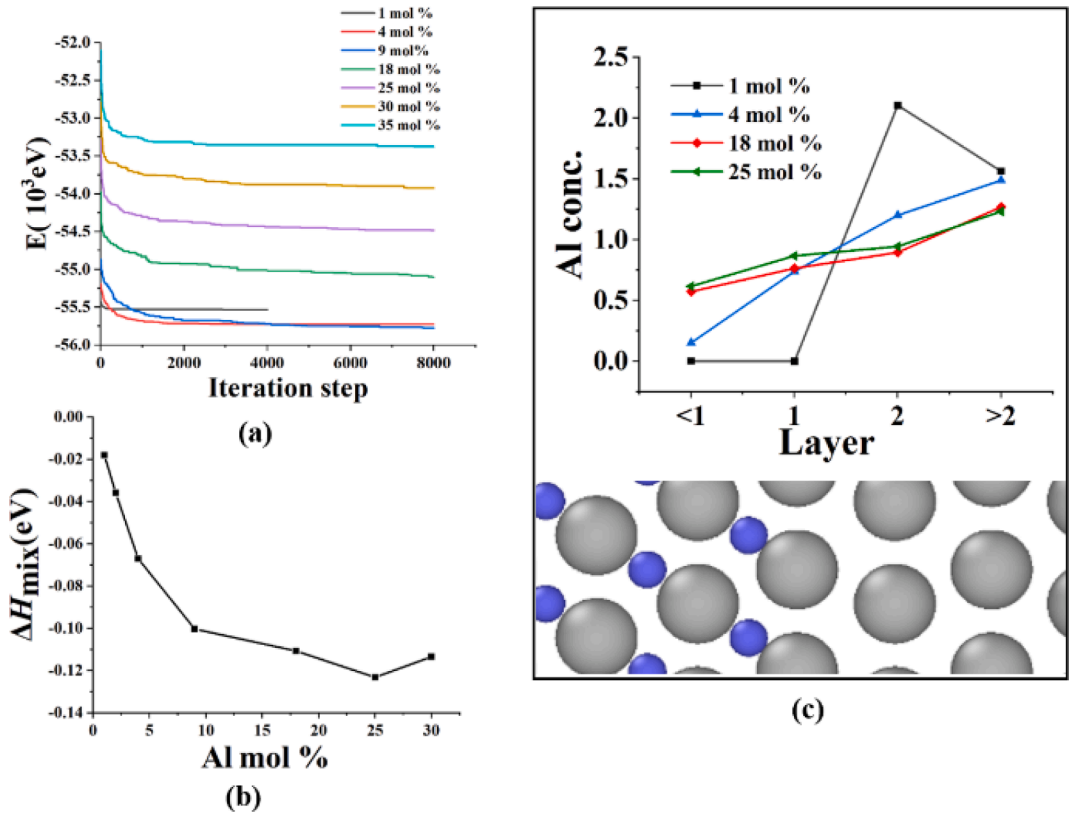

Fig. 5. (a) Plot of the energy with respect to MC step (b) Enthalpy of mixing of various Al doped Ti/TiN metal/ceramic systems (c) Aluminum composition in each Ti layer of Ti/TiN system with the snapshot below the figure showing the position of each layer.

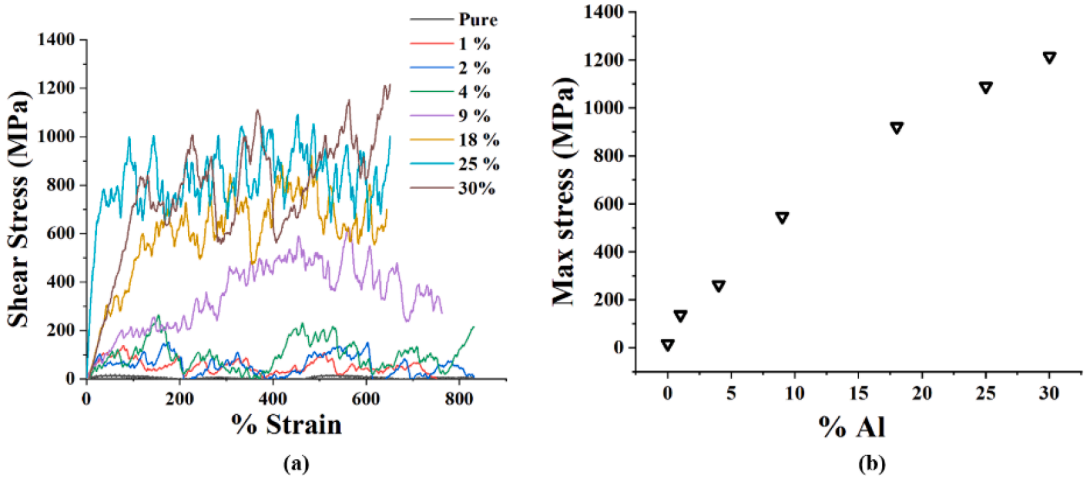

Fig. 6. (a) Plots of shear stress versus strain for different Al compositions, and (b) maximum shear stress achieved for the different Al compositions in Ti/TiN interfacial systems.

metal phase) coinciding with the snapshot at the bottom third of the fig. A value of 1.0 in Al composition represents the overall average of Al composition with respect to all of the Ti atoms in the system. So, if the Al atoms are evenly distributed, there will be a value of 1.0 throughout at any mol % of Al. For the system with 1 mol% Al, there is essentially zero Al atoms in the TiN phase or in the metal layer adjacent to the TiN surface, while the most likely position to find one is in layer two. This is consistent with the previous DFT calculations when one or two Al atoms were present [10]. At all higher Al compositions, the probability to find Al atoms in layer two becomes lower than in bulk Ti, showing that the higher Al composition in layer two is only present for the lowest overall composition. Al atoms do not significantly accumulate in layer one or in the TiN phase until 4 mol% is reached, showing that this is also a consequence of higher composition.

3.3.2. *Interfacial shear*

The shear strength was calculated by using a stress-controlled shear loading with quasi-static loading applied in the X direction as described previously [67]. The method used incremental deformation gradients separately applied to the metal and ceramic phase based on their stresses, which were implemented in the X || $[11\bar{2}0]_{Ti}$ || $[1\bar{1}0]_{TiN}$ direction, followed by energy minimization at fixed deformation. During

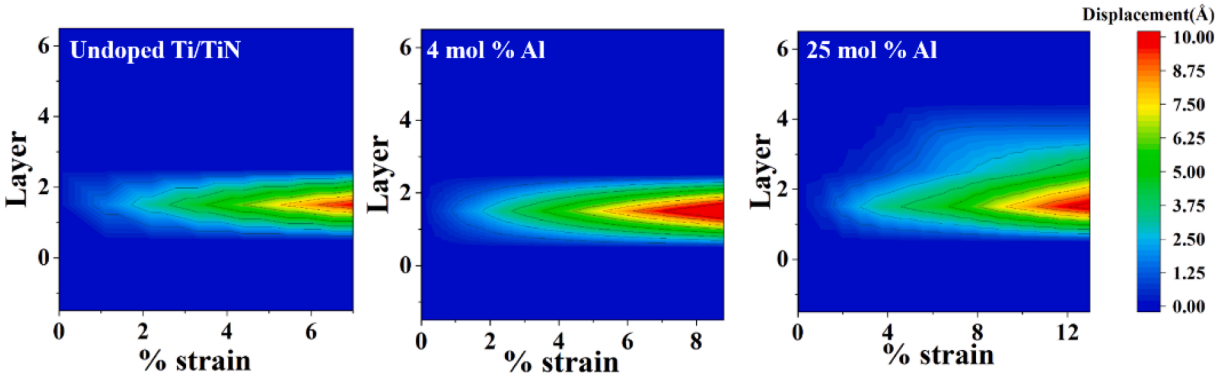

Fig. 7. Snapshots of displacement for various layers of Al doped Ti/TiN surfaces.

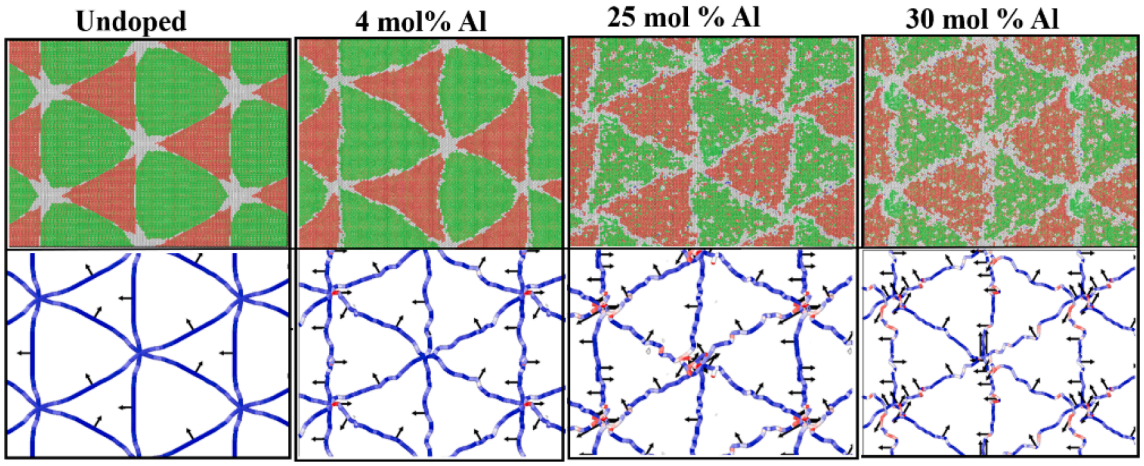

Fig. 8. Snapshots of various Al doped Ti/TiN surfaces using common neighbor analysis (top) to classify fcc (green), hcp (red), and amorphous (amorphous). Dislocation and Burgers vector analysis of various Al doped Ti/TiN systems (bottom) with black arrows indicating Burgers vectors, blue lines indicating edge dislocations, and red line indicating screw dislocations. The horizontal direction is the X dimension described in section 2.4 and the vertical directions is the Y dimension. (For interpretation of the references to colour in this figure legend, the reader is referred to the web version of this article.)

each incremental deformation gradient, a 1 ps NVT simulation at 5 K was run, followed by a full relaxation of the cell structure and atomic positions, minimizing the total energy at fixed strain. The methodology is identical to previous work [40]. Fig. 6(a) shows the plot of shear stress in the various Al doped Ti/TiN systems as a function of strain. The results for the undoped system are taken from previous work [40], which indicated an extremely low shear strength. By increasing Al composition, the shear strength increases rapidly with strain up to the point of starting plastic deformation. For the doped systems, this appeared to be around 2% of strain. To better compare how the amount of doping impacts shear stress, Fig. 6(b) shows the maximum shear stress as a function of Al composition. The value for the undoped system is small, almost unimpeded due to the presence of the MDN and the low GSFE barrier near the Ti/TiN interface [40]. When the Al composition is raised slightly, the shear stress increases considerably to over 150 MPa, and it continues to increase at an almost linear rate with higher Al mol % until the strength is >1 GPa at 25 Al mol %.

To determine specifically where shear failure occurs, the displacement was calculated as a function of strain for each layer near the metal/ceramic interface. Specifically, the displacement difference between adjacent layers was calculated, which is shown in Fig. 7 for the undoped interface, the system with 4 mol% of Al and the system with 25 mol% of Al. The maximum strain shown in the plots was set to the point where the maximum displacement reached 10 Å for each system. This was around 10% strain for the three systems examined, with higher values correlated with higher Al composition. For all systems, the initial displacement occurs between the first and second layer next to the Ti/TiN interface. This continues for the undoped and 4 mol% system, with all displacements occurring in the first layer throughout the length of the simulations. For the 25 mol% system, though, displacements start to occur two layers from the interface, starting around 4% strain. This coincides with a region where the stress increases rapidly as shown in Fig. 6(a).

As shear failure occurs between the first and second Ti layers from the interface, the structure of the second layer was further investigated. Snapshots extracted from equilibrium structures from the Ovito software [68], in which the common neighbor analysis was used to identify hcp (red), fcc (green), and amorphous regions (white) are shown for the undoped, along with the 4, 25, and 30 Al mol % systems in Fig. 8. The undoped Ti/TiN system is similar to what has been found in previous work [26], showing interdispersed fcc and hcp triangles with moderately sized nodes at their vertices. For the 4 mol% Al doped system, the size of the nodes decreases, and the shape of the nodes and hcp regions become less defined. The smaller nodes are consistent with the higher GSFE barriers present when Al atoms are added to Ti/TiN (see Fig. 4). These smaller nodes should result in greater pinning effects [67], which is likely the reason for the increased shear strength with higher Al composition.

For the 25 mol% Al system, it is difficult to discern if the node size becomes smaller, pointing to another likely mechanism for the order of magnitude increase in shear strength for this system in comparison with the 4 mol% one. Fig. 8 also shows the presence of edge and screw dislocations in the second layer from the Ti/TiN interface for the different systems. The edge and screw type dislocations are calculated using the

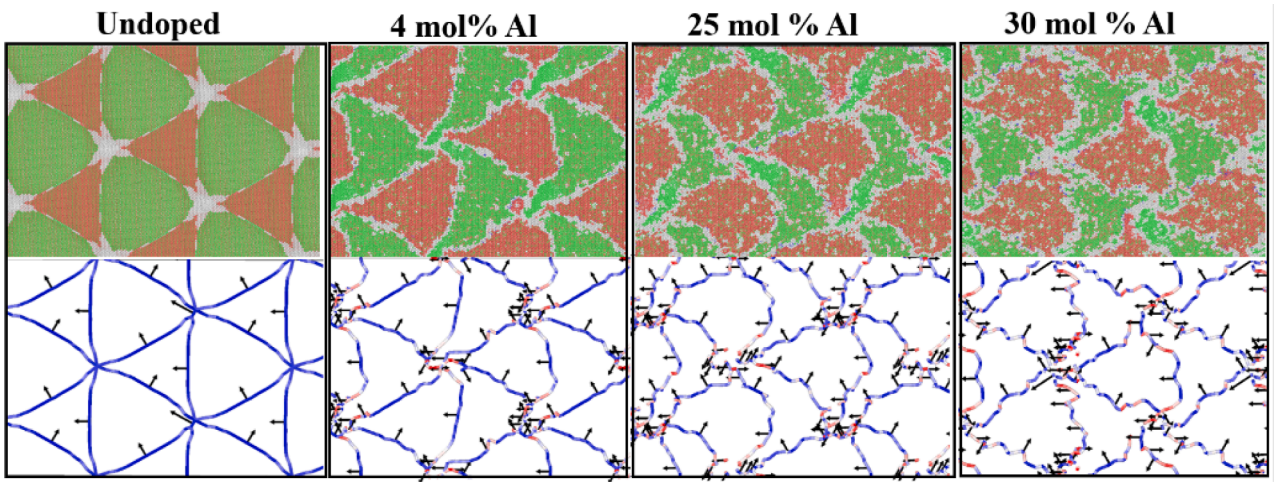

Fig. 9. Snapshots of various Al doped Ti/TiN surfaces (top) and corresponding dislocation and Burgers vector analysis (bottom) for the same systems shown in Fig. 8, but at the barrier for shear failure with displacement to the right. The colors and arrows correspond to the same information shown in Fig. 8.

dislocation analysis implemented in the OVITO program as described in the reference [69]. The undoped system only has edge dislocations present, and for the most part, the 4 mol% system only has the same defects. For both the 25 and 30 mol% systems, though, there are significant screw dislocations present, which is likely the reason for the displacements in the third layer from the interface for this system only (see Fig. 7). It appears that the alloying Al atoms in the host Ti matrix, along with the defects that occur as a result of them, interact with the dislocations and provide resistance to motion [70]. The larger number of screw dislocations caused by these interactions further impedes shear deformation resulting in the large increase in shear strength for the 25 and 30 mol% systems [71],[72].

To better understand the microstructure at the barrier for shear failure, Fig. 9 shows snapshots and the same dislocation analysis described in Fig. 8, but at the barrier for shear failure. The undoped structure at the barrier is nearly identical to the minimum energy configuration, with the node shape and size, along with the shape of the crystalline regions, being the same. For the 4 mol% system, the node present in the minimum energy structure is not present at the barrier, but some screw dislocations are present where the nodes in the minimum energy structure were located. Additionally, the shapes of the crystalline regions are distorted away from where the nodes are present in the minimum energy structure, showing the pinning effect of the node positions for the 4 mol% system. For the 25 and 30 mol% systems, similar qualitative behavior at the barrier for shear failure is present as for the 4 mol% system, but to a greater degree, which is consistent with the greater shear strength of these systems, along with greater number of layers displaced as shown in Fig. 7.

4. Conclusion

A new interatomic MEAM potential for Ti-Al-N interactions was developed to examine the effect of the addition of Al on the shear strength of the Ti/TiN interface. The Ti, N, and TiN interactions were taken from a previously developed MEAM potential for Ti/TiN, with the Al unary, AlN and AlTi binary, and TiAlN ternary interactions parameterized for this work. A previously developed genetic algorithm code was utilized to fit the model to reproduce a combination of DFT and experimental properties. A Monte Carlo minimization procedure was implemented to find low energy configurations of Al doped Ti/TiN at various Al compositions. The structure and shear strength of the Ti (0001)/TiN(111) interface was investigated with misfit dislocation networks (MDNs) present in the second metal layer from the Ti/TiN interface (with the TiN nitrogen oriented towards the Ti phase) in both directions parallel to the interface. It was found that the presence of Al significantly increased the shear strength of the Ti/TiN interface, by two orders of magnitude. Shear failure occurred between the first and second metal layers from the TiN interface. Previous work found that large nodes formed at the Ti/TiN interface, while the current work found that small compositions of Al shrunk the size of these nodes to a significant degree, increasing their pinning effect and overall shear strength. At higher Al compositions, the presence of screw dislocations impeded atomic movement, further increasing the interfacial shear strength.

CRediT authorship contribution statement

Nisha Dhariwal: Writing – original draft, Investigation, Data curation, Formal analysis. **Abu Shama Mohammad Miraz:** Investigation. **W.J. Meng:** Funding acquisition, Conceptualization. **Collin D. Wick:** Supervision, Methodology, Writing – review & editing.

Declaration of Competing Interest

The authors declare the following financial interests/personal relationships which may be considered as potential competing interests:

Collin Wick reports some financial support were provided by National Science Foundation

Data availability

Data will be made available on request.

Acknowledgment

The current work was funded by the United States National Science Foundation under cooperative agreements OIA-1541079 and OIA-1946231. The high-performance computing resources provided by the Louisiana Optical Network Infrastructure (https://loni.org) were used for this work.

Appendix A. Supplementary data

Supplementary data to this article can be found online at https://doi.org/10.1016/j.apsusc.2022.156024.

References

[1] N. Li, X.-Y. Liu, Review: mechanical behavior of metal/ceramic interfaces in nanolayered composites—experiments and modeling, J. Mater. Sci. 53 (2017) 5562–5583, https://doi.org/10.1007/s10853-017-1767-1.

[2] S.B. Sinnott, E.C. Dickey, Ceramic/metal interface structures and their relationship to atomic- and meso-scale properties, Mater. Sci. Eng. R. Rep. 43 (2003) 1–59, https://doi.org/10.1016/j.mser.2003.09.001.

[3] N.P. Padture, Thermal barrier coatings for gas-turbine engine applications, Science 296 (2002) (1979) 280–284, https://doi.org/10.1126/science.1068609.

[4] A. Leyland, A. Matthews, On the significance of the H/E ratio in wear control: a nanocomposite coating approach to optimised tribological behaviour, Wear. 246 (2000) 1–11, https://doi.org/10.1016/s0043-1648(00)00488-9.

[5] H. Bian, X. Song, S. Hu, Y. Lei, Y. Jiao, S. Duan, J. Feng, W. Long, Microstructure evolution and mechanical properties of titanium/alumina brazed joints for medical implants, Metals (Basel). 9 (2019) 644, https://doi.org/10.3390/met9060644.

[6] M.C. Halbig, M.H. Jaskowiak, J.D. Kiser, D. Zhu, Evaluation of ceramic matrix composite technology for aircraft turbine engine applications, in: 51st AIAA Aerospace Sciences Meeting Including the New Horizons Forum and Aerospace Exposition 2013, 2013, https://doi.org/10.2514/6.2013-539.

[7] H.C. Lee, K. Kim, S.Y. Han, S.K. Choi, E. Lee, M. Jo, M.S. Yoo, K. Cho, Highly conductive flexible metal-ceramic nanolaminate electrode for high-performance soft electronics, ACS Appl. Mater. Interfaces 11 (2019) 2211–2217, https://doi.org/10.1021/acsami.8b14821.

[8] D.A. Chance, D.L. Wilcox, Metal-ceramic constraints for multilayer electronic packages, Proc. IEEE 59 (1971) 1455–1462, https://doi.org/10.1109/PROC.1971.8454.

[9] A. Khubaev, T. Bidov, A. Bzhienikov, V.V. Karakulov, Y. Smolin, S.N. Kulkov, Y. Long, N.X. Chen, W.Q. Zhang, M.W. Finnis, The theory of metal - ceramic interfaces, J. Phys. Condens. Matter 8 (1996) 5811, https://doi.org/10.1088/0953-8984/8/32/003.

[10] A.S.M. Miraz, E. Williams, W.J. Meng, B.R. Ramachandran, C.D. Wick, Improvement of Ti/TiN interfacial shear strength by doping – a first principles density functional theory study, Appl. Surf. Sci. 517 (2020), 146185, https://doi.org/10.1016/j.apsusc.2020.146185.

[11] F. Spaepen, Interfaces and stresses in thin films, Acta Mater. 48 (2000) 31–42, https://doi.org/10.1016/s1359-6454(99)00286-4.

[12] M. Humenik, W.D. Kingery, Metal-ceramic interactions: III, surface tension and wettability of metal-ceramic systems, J. Am. Ceram. Soc. 37 (1954) 18–23, https://doi.org/10.1111/J.1151-2916.1954.TB13972.X.

[13] E.A.A. Jarvis, E.A. Carter, An atomic perspective of a doped metal-oxide interface, J. Phys. Chem. B 106 (2002) 7995–8004, https://doi.org/10.1021/JP0257348.

[14] A.G. Evans, J.W. Hutchinson, Y. Wei, Interface adhesion: effects of plasticity and segregation, Acta Mater. 47 (1999) 4093–4113, https://doi.org/10.1016/s1359-6454(99)00269-4.

[15] W. Zhang, J.R. Smith, Nonstoichiometric interfaces andAl2O3Adhesion with Al and ag, Phys. Rev. Lett. 85 (2000) 3225–3228, https://doi.org/10.1103/physrevlett.85.3225.

[16] D.J. Siegel, L.G. Hector, J.B. Adams, First-principles study of metal–carbide/nitride adhesion: Al/VC vs. Al/VN, Acta Mater. 50 (2002) 619–631, https://doi.org/10.1016/s1359-6454(01)00361-5.

[17] I.J. Bennett, J.M. Kranenburg, W.G. Sloof, Modeling the influence of reactive elements on the work of adhesion between oxides and metal alloys, J. Am. Ceram. Soc. 88 (2005) 2209–2216, https://doi.org/10.1111/J.1551-2916.2005.00408.X.

[18] H.S. Abdelkader, H.I. Faraoun, C. Esling, Effects of rhenium alloying on adhesion of Mo/HfC and Mo/ZrC interfaces: a first-principles study, J. Appl. Phys. 110 (2011), 044901, https://doi.org/10.1063/1.3624580.

[19] C.A. Leon, V.H. Lopez, E. Bedolla, R.A.L. Drew, Wettability of TiC by commercial aluminum alloys, J. Mater. Sci. 37 (2002) 3509–3514, https://doi.org/10.1023/A:1016523408906.

[20] H.F. Fischmeister, G. Elssner, B. Gibbesch, K.H. Kadow, F. Kawa, D. Korn, W. Mader, M. Turwitt, Solid-state bonding of accurately oriented metal/ceramic bicrystals in ultrahigh vacuum, Rev. Sci. Instrum. 64 (1998) 234, https://doi.org/10.1063/1.1144443.

[21] J.R. Smith, T. Hong, D.J. Srolovitz, Metal-ceramic adhesion and the Harris functional, Phys. Rev. Lett. 72 (1994) 4021, https://doi.org/10.1103/PhysRevLett.72.4021.

[22] T. Hong, J.R. Smith, D.J. Srolovitz, Theory of metal—ceramic adhesion, Acta Metall. Mater. 43 (1995) 2721–2730, https://doi.org/10.1016/0956-7151(94)00457-S.

[23] T. Sun, X. Wu, W. Li, R. Wang, The mechanical and electronic properties of Al/TiC interfaces alloyed by Mg, Zn, Cu, Fe and Ti: First-principles study, Phys. Scr. 90 (2015), 035701, https://doi.org/10.1088/0031-8949/90/3/035701.

[24] H. Hui Xiong, H. Hua Zhang, H. Ning Zhang, Y. Zhou, Effects of alloying elements X (X=Zr, V, Cr, Mn, Mo, W, Nb, Y) on ferrite/TiC heterogeneous nucleation interface: first-principles study, J. Iron Steel Res. Int. 24 (3) (2017) 328–334, https://doi.org/10.1016/S1006-706X(17)30047-X.

[25] H.Z. Zhang, S.Q. Wang, The effects of Zn and Mg on the mechanical properties of the Al/TiN interface: a first-principles study, J. Phys. Condens. Matter 19 (2007), 226003, https://doi.org/10.1088/0953-8984/19/22/226003.

[26] A.S.M. Miraz, W.J. Meng, B.R. Ramachandran, C.D. Wick, Computational observation of the strengthening of Cu/TiN metal/ceramic interfaces by sub-nanometer interlayers and dopants, Appl. Surf. Sci. 554 (2021), 149562, https://doi.org/10.1016/J.APSUSC.2021.149562.

[27] E.A. Jarvis, E.A. Carter, Importance of open-shell effects in adhesion at metal-ceramic interfaces, Phys. Rev. B 66 (2002), 100103, https://doi.org/10.1103/PhysRevB.66.100103.

[28] M. Damadam, S. Shao, I. Salehinia, G. Ayoub, H.M. Zbib, Molecular dynamics simulations of mechanical behavior in nanoscale ceramic–metallic multilayer composites, Http://Mc.Manuscriptcentral.Com/Tmrl. 5 (2017) 306–313, https://doi.org/10.1080/21663831.2016.1275864.

[29] M.I. Baskes, Application of the embedded-atom method to covalent materials: a semiempirical potential for silicon, Phys. Rev. Lett. 59 (1987) 2666–2669, https://doi.org/10.1103/physrevlett.59.2666.

[30] M.S. Daw, M.I. Baskes, Embedded-atom method: derivation and application to impurities, surfaces, and other defects in metals, Phys. Rev. B 29 (1984) 6443–6453, https://doi.org/10.1103/physrevb.29.6443.

[31] M.I. Baskes, R.A. Johnson, Modified embedded atom potentials for HCP metals, Model. Simul. Mater. Sci. Eng. 2 (1994) 147–163, https://doi.org/10.1088/0965-0393/2/1/011.

[32] M.I. Baskes, J.S. Nelson, A.F. Wright, Semiempirical modified embedded-atom potentials for silicon and germanium, Phys. Rev. B 40 (1989) 6085–6100, https://doi.org/10.1103/physrevb.40.6085.

[33] M.S. Daw, S.M. Foiles, M.I. Baskes, The embedded-atom method: a review of theory and applications, Mater. Sci. Rep. 9 (1993) 251–310, https://doi.org/10.1016/0920-2307(93)90001-u.

[34] B.-J. Lee, W.-S. Ko, H.-K. Kim, E.-H. Kim, The modified embedded-atom method interatomic potentials and recent progress in atomistic simulations, Calphad. 34 (2010) 510–522, https://doi.org/10.1016/j.calphad.2010.10.007.

[35] X. Yuan, K. Takahashi, Y. Yin, T. Onzawa, Development of modified embedded atom method for a bcc metal: lithium, Model. Simul. Mater. Sci. Eng. 11 (2003) 447–456, https://doi.org/10.1088/0965-0393/11/4/303.

[36] S.M. Foiles, M.I. Baskes, M.S. Daw, Embedded-atom-method functions for the fcc metals Cu, Ag, Au, Ni, Pd, Pt, and their alloys, Phys. Rev. B 33 (1986) 7983–7991, https://doi.org/10.1103/physrevb.33.7983.

[37] S. Ding, X. Wang, A systematic study on the MEAM interatomic potentials of the transition metal nitrides TMNs (TM=Ti, V, Cr, Fe) binary systems, J. Alloys Compd. 805 (2019) 1081–1089, https://doi.org/10.1016/j.jallcom.2019.07.114.

[38] B. Narayanan, K. Sasikumar, Z.G. Mei, A. Kinaci, F.G. Sen, M.J. Davis, S.K. Gray, M. K.Y. Chan, S.K.R.S. Sankaranarayanan, Development of a modified embedded atom force field for zirconium nitride using multi-objective evolutionary optimization, J. Phys. Chem. C 120 (2016) 17475–17483, https://doi.org/10.1021/acs.jpcc.6b05296.

[39] Y.-M. Kim, B.-J. Lee, Modified embedded-atom method interatomic potentials for the Ti–C and Ti–N binary systems, Acta Mater. 56 (2008) 3481–3489, https://doi.org/10.1016/j.actamat.2008.03.027.

[40] A.S.M. Miraz, N. Dhariwal, W.J. Meng, B.R. Ramachandran, C.D. Wick, Development and application of interatomic potentials to study the stability and shear strength of Ti/TiN and Cu/TiN interfaces, Mater. Des. 196 (2020), 109123, https://doi.org/10.1016/j.matdes.2020.109123.

[41] E.Y. Chen, R. Dingreville, C. Deo, Misfit dislocation networks in semi-coherent miscible phase boundaries: an example for U–Zr interfaces, Comput. Mater. Sci. 154 (2018) 194–203, https://doi.org/10.1016/j.commatsci.2018.07.065.

[42] D. Cheng, Z.J. Yan, L. Yan, Misfit dislocation network in Cu/Ni multilayers and its behaviors during scratching, Thin Solid Films 515 (2007) 3698–3703, https://doi.org/10.1016/j.tsf.2006.10.001.

[43] R. Namakian, B.R. Novak, X. Zhang, W.J. Meng, D. Moldovan, A combined molecular dynamics/Monte Carlo simulation of Cu thin film growth on TiN substrates: illustration of growth mechanisms and comparison with experiments, Appl. Surf. Sci. 570 (2021), https://doi.org/10.1016/J.APSUSC.2021.151013.

[44] B.-J. Lee, M.I. Baskes, Second nearest-neighbor modified embedded-atom-method potential, Phys. Rev. B 62 (2000) 8564–8567, https://doi.org/10.1103/physrevb.62.8564.

[45] J.H. Rose, J.R. Smith, F. Guinea, J. Ferrante, Universal features of the equation of state of metals, Phys. Rev. B 29 (1984) 2963–2969, https://doi.org/10.1103/physrevb.29.2963.

[46] B.-J. Lee, M.I. Baskes, H. Kim, Y. Koo Cho, Second nearest-neighbor modified embedded atom method potentials for bcc transition metals, Phys. Rev. B 64 (2001), https://doi.org/10.1103/physrevb.64.184102.

[47] Y.-K. Kim, H.-K. Kim, W.-S. Jung, B.-J. Lee, Atomistic modeling of the Ti–Al binary system, Comput. Mater. Sci. C. (2016) 1–8, https://doi.org/10.1016/J.COMMATSCI.2016.03.038.

[48] S. Sun, B.R. Ramachandran, C.D. Wick, Solid, liquid, and interfacial properties of TiAl alloys: parameterization of a new modified embedded atom method model, J. Phys. Condens. Matter 30 (2018), 075002, https://doi.org/10.1088/1361-648x/aaa52c.

[49] G. Kresse, J. Furthmüller, Efficient iterative schemes for ab initio total-energy calculations using a plane-wave basis set, Phys. Rev. B Condens. Matter. Mater. Phys. 54 (1996) 11169–11186, https://doi.org/10.1103/PhysRevB.54.11169.

[50] J.P. Perdew, K. Burke, M. Ernzerhof, Generalized gradient approximation made simple, Phys. Rev. Lett. 77 (1996) 3865–3868, https://doi.org/10.1103/physrevlett.77.3865.

[51] J. Hafner, Ab-initiosimulations of materials using VASP: density-functional theory and beyond, J. Comput. Chem. 29 (2008) 2044–2078, https://doi.org/10.1002/jcc.21057.

[52] D. Joubert, From ultrasoft pseudopotentials to the projector augmented-wave method, Phys. Rev. B Condens. Matter. Mater. Phys. 59 (1999) 1758–1775, https://doi.org/10.1103/PhysRevB.59.1758.

[53] H.J. Monkhorst, J.D. Pack, Special points for Brillouin-zone integrations, Phys. Rev. B 13 (1976) 5188–5192, https://doi.org/10.1103/physrevb.13.5188.

[54] A.S. Mohammad Miraz, S. Sun, S. Shao, W.J. Meng, B.R. Ramachandran, C. D. Wick, Computational study of metal/ceramic interfacial adhesion and barriers to shear displacement, Comput. Mater. Sci. 168 (2019) 104–115, https://doi.org/10.1016/j.commatsci.2019.06.006.

[55] S. Plimpton, Fast parallel algorithms for short-range molecular dynamics, J. Comput. Phys. 117 (1995) 1–19, https://doi.org/10.1006/jcph.1995.1039.

[56] W.G. Hoover, Canonical dynamics: equilibrium phase-space distributions, Phys. Rev. A (Coll Park). 31 (1985) 1695–1697, https://doi.org/10.1103/PhysRevA.31.1695.
[57] S. Nosé, A unified formulation of the constant temperature molecular dynamics methods, J. Chem. Phys. 81 (1984) 511–519, https://doi.org/10.1063/1.447334.
[58] J. Akola, H. Häkkinen, M. Manninen, Ionization potential of aluminum clusters, Phys. Rev. B 58 (1998) 3601, https://doi.org/10.1103/PhysRevB.58.3601.
[59] G.E. Totten, D.S. MacKenzie, Handbook of aluminum, in: Physical Metallurgy and Processes vol. 1, CRC Press, 2003. https://books.google.com/books?id=Wbwv3nt1gp0C.
[60] N. Dhariwal, A.S.M. Miraz, W.J. Meng, B.R. Ramachandran, C.D. Wick, Impact of metal/ceramic interactions on interfacial shear strength: study of Cr/TiN using a new modified embedded-atom potential, Mater. Des. 210 (2021), 110120, https://doi.org/10.1016/J.MATDES.2021.110120.
[61] H.E. Schaefer, R. Gugelmeier, M. Schmolz, A. Seeger, Positron lifetime spectroscopy and trapping at vacancies in aluminium, Mater. Sci. Forum 15–18 (1987) 111–116, https://doi.org/10.4028/WWW.SCIENTIFIC.NET/MSF.15-18.111.
[62] W.M. Haynes, CRC Handbook of Chemistry and Physics, 92nd ed., 2012. Boca Raton, FL, https://www.amazon.com/CRC-Handbook-Chemistry-Physics-92nd/dp/1439855110.
[63] P. Villars, P. Villars, Pearson's Handbook : Crystallographic Data for Intermetallic Phases, Desk ed., ASM International, Materials Park OH, 1997.
[64] K. Tanaka, T. Ichitsubo, H. Inui, M. Yamaguchi, M. Koiwa, Single-crystal elastic constants of gamma-TiAl, Philos. Mag. Lett. 73 (1996) 71–78, https://doi.org/10.1080/095008396181019.
[65] K. Tanaka, K. Okamoto, H. Inul, Y. Mlnonishl, M. Yamaguch, M. Koiwa, Elastic constants and their temperature dependence for the intermetallic compound Ti3Al 73, 2006, pp. 1475–1488, https://doi.org/10.1080/01418619608245145.
[66] M. Nakamura, K. Kimura, Elastic constants of TiAl3 and ZrAl3 single crystals, J. Mater. Sci. 26 (8) (1991) 2208–2214, https://doi.org/10.1007/BF00549190.
[67] X. Zhang, B. Zhang, Y. Mu, S. Shao, C.D. Wick, B.R.R. Ramachandran, W.J. Meng, Mechanical failure of metal/ceramic interfacial regions under shear loading, Acta Mater. 138 (2017) 224–236, https://doi.org/10.1016/j.actamat.2017.07.053.
[68] A. Stukowski, Structure identification methods for atomistic simulations of crystalline materials, Model. Simul. Mater. Sci. Eng. 20 (2012) 45021, https://doi.org/10.1088/0965-0393/20/4/045021.
[69] A. Stukowski, Visualization and analysis of atomistic simulation data with OVITO–the open visualization tool, Model. Simul. Mater. Sci. Eng. 18 (2009), 015012, https://doi.org/10.1088/0965-0393/18/1/015012.
[70] R.S. Mishra, N. Kumar, M. Komarasamy, Lattice strain framework for plastic deformation in complex concentrated alloys including high entropy alloys 31, 2015, pp. 1259–1263, https://doi.org/10.1179/1743284715Y.0000000050.
[71] P. Kwasniak, H. Garbacz, Screw dislocation mediated solution strengthening of substitutional α-Ti alloys - First principles investigation, Acta Mater. 141 (2017) 405–418, https://doi.org/10.1016/j.actamat.2017.09.028.
[72] P. Kwasniak, H. Garbacz, K.J. Kurzydlowski, Solid solution strengthening of hexagonal titanium alloys: restoring forces and stacking faults calculated from first principles, Acta Mater. 102 (2016) 304–314, https://doi.org/10.1016/J.ACTAMAT.2015.09.041.

Supplementary Information

A Molecular Dynamics study of the impact of Al doping on the Ti/TiN interfacial strength

Nisha Dhariwal,[1] Abu Shama Mohammad Miraz,[1] W. J. Meng,[2] Collin D. Wick[1]

[1]*College of Engineering & Science, Louisiana Tech University, Ruston, Louisiana 71272, USA.*

[2]*Department of Mechanical & Industrial Engineering, Louisiana State University*

Baton Rouge, Louisiana 70803, USA.

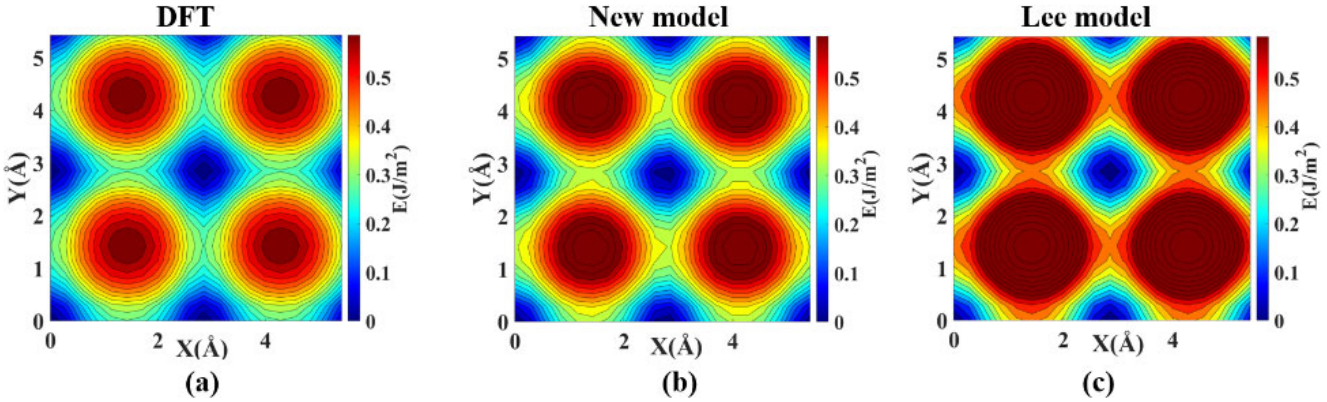

Figure S1: GSFE curves of the Al(001) calculated using (a) DFT, (b) MEAM model (c) Lee model

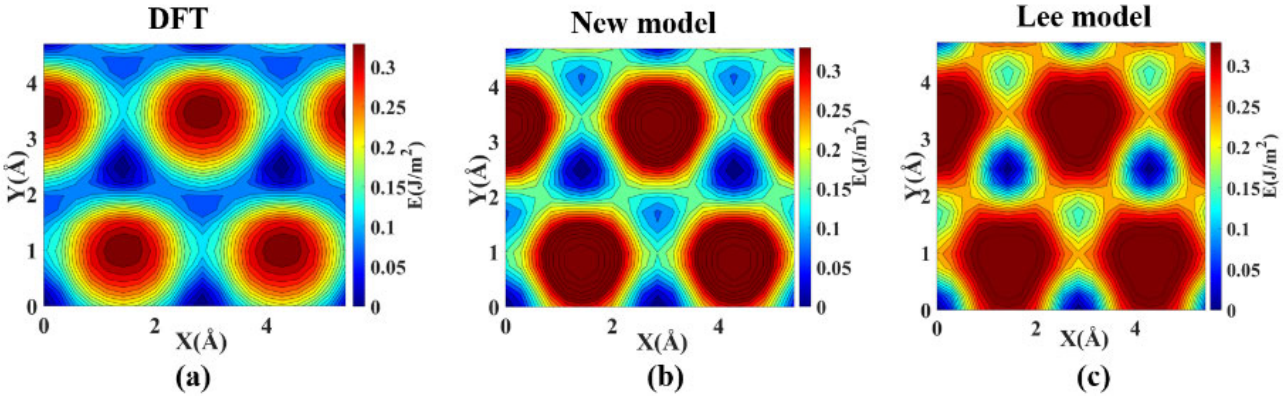

Figure S2: GSFE curves of the Al(111) calculated using (a) DFT, (b) MEAM model (c) Lee model

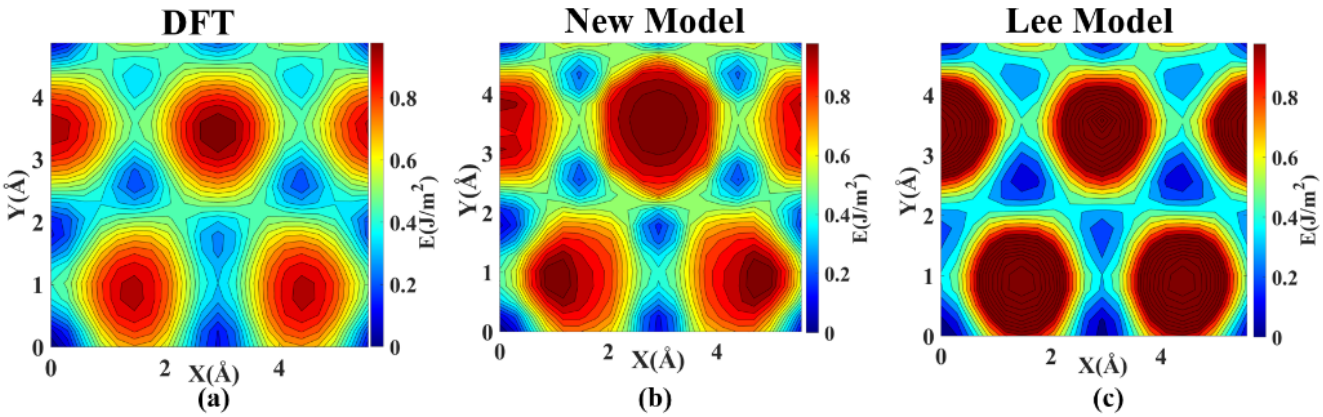

Figure S3: 2D GSFE plots of the Al doped bulk Ti using (a) DFT, (b) MEAM model and (c) Lee model.

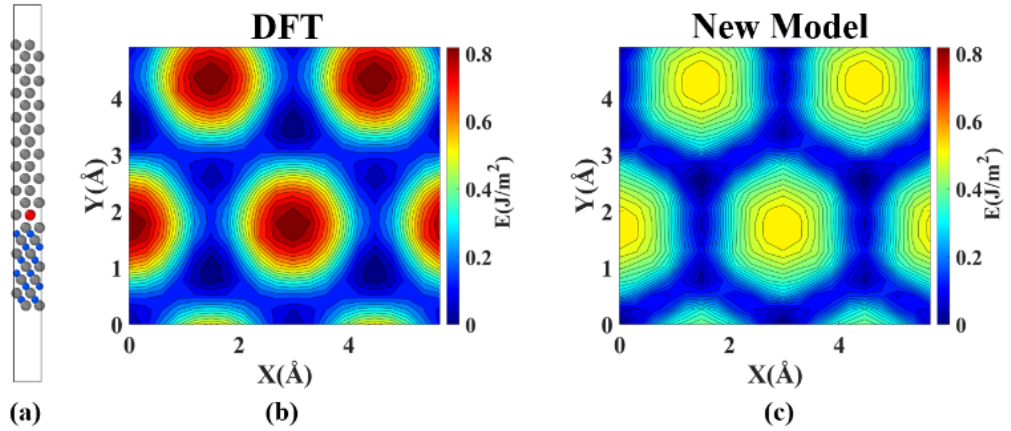

Figure S4: 2D GSFE plots of the Ti/TiN system with 1 Al atom in M =2 layer using (a) DFT and (b) new MEAM model.

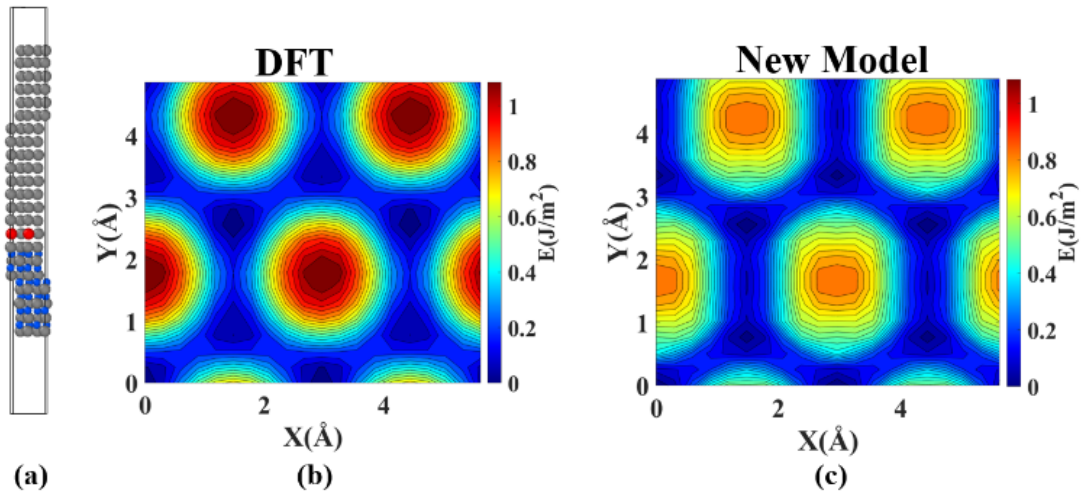

Figure S5: 2D GSFE plots of the Ti/TiN system with 2 Al atoms in M =2 layer using (a) DFT and (b) new MEAM model.

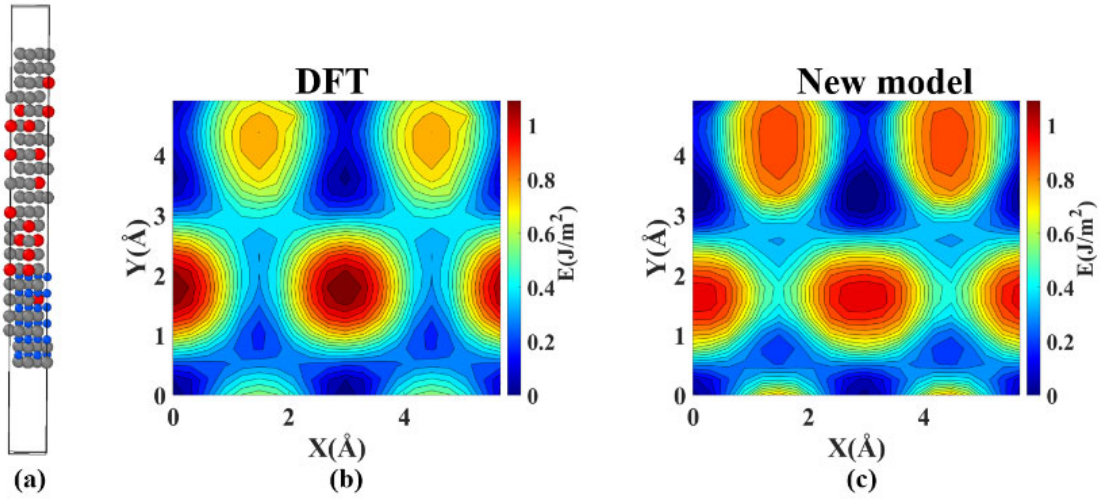

Figure S6: 2D GSFE plots of the Ti/TiN system with 16 Al atoms using (a) DFT and (b) new MEAM model.